Lab on a Chip

Devices and applications at the micro- and nanoscale

rsc.li/loc

ROYAL SOCIETY
OF **CHEMISTRY**

PAPER
Jürgen Popp *et al.*
Image-based fuzzy logic control for pressure-driven
droplet microfluidics as autosampler for multimodal
imaging microscopy

Image-based fuzzy logic control for pressure-driven droplet microfluidics as autosampler for multimodal imaging microscopy†

Fabian Ott,[a] Tobias Meyer-Zedler, [iD] [a] Michael Schmitt [iD] [b] and Jürgen Popp [iD] *[ab]

Here we present a highly customisable image-based fuzzy logic control (FLC) method for pressure-driven droplet microfluidics. The system is designed to position droplets of different sizes in microfluidic chips of varying channel size in the centre of the region of interest (ROI) using two parallel multiple input single output (MISO) FLCs. Overall, 95.1% of the droplets with an average displacement of 2.5 µm could be kept within the ROI during the pre-defined time intervals of up to 10 s. This is achieved by pre-determined pressure values that are kept constant during this time. The control principle was tested on different pressure controllers and microfluidic chips varying in material, channel layout and cross section. Droplet volumes ranged from a few hundred picolitres to a tenth of a microlitre. The droplets were composed of deionised water or contained two concentrations of *S. cerevisiae*. The average processing time was 12.5 seconds. This makes the method suitable for studying several hundred pre-sorted droplets from high-throughput screening (HTS) experiments.

Introduction

Droplet microfluidics is ideal for manipulating and analyzing small volumes of fluids and the analytes they contain. The principle is based on the immiscibility of a continuous and a disperse phase, making each droplet a confined reaction chamber.[1-3] The technique combined with appropriate microfluidic chips and pressure controllers, enables the generation of monodisperse droplets of precisely defined size and composition.[4-6] The droplet volume produced is determined by the channel geometry, pressure difference (ΔP) between continuous and disperse phases, interfacial tension, viscosities and surfactants.[7-10] Ultimately, the application determines the droplet size, which ranges from picolitres to microlitres. By covering several orders of magnitude, a wide range of applications in chemistry, biology, materials science and diagnostics can be addressed.[11-14]

Parallel monitoring of large number of droplets can be performed in observation chambers for longer periods of time.[15] In contrast the aim of this work is to automatically analyze and move individual droplets of interest for longer time spans. To combine droplet microfluidics with different microscopic imaging modalities, it is necessary to overcome the obstacle of their different operating and acquisition frequencies. In general, pressure-driven droplet microfluidics means continuous generation of droplets at constant velocity and kHz rates.[16] This requires the use of high-speed cameras

[a] Member of Leibniz Health Technologies, Member of the Leibniz Center for Photonics in Infection Research (LPI), Leibniz Institute of Photonic Technology (Leibniz-IPHT), Albert-Einstein-Str. 9, 07745 Jena, Germany
[b] Institute of Physical Chemistry (IPC) and Abbe Center of Photonics (ACP), Member of the Leibniz Center for Photonics in Infection Research (LPI), Friedrich Schiller University Jena, Helmholtzweg 4, 07743 Jena, Germany. E-mail: juergen.popp@uni-jena.de

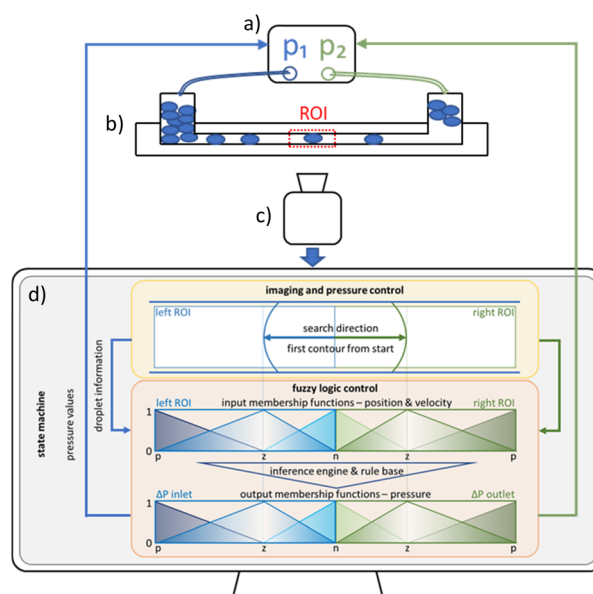† Electronic supplementary information (ESI) available. See DOI: https://doi.org/10.1039/d4lc00583j

Fig. 1 Basic operation principle, a) pressure controller, b) microfluidic chip with sample reservoirs for pre-sorted droplets, c) microscope camera, d) image processing and FLC algorithm.

with correspondingly short exposure times to avoid motion blur.[17] The flow rate of the droplets is subject to certain fluctuations[18] and vortices form within the droplets.[19,20] Therefore, measurements that require switching between widefield and confocal imaging modalities with long acquisition times are extremely challenging.

However, there are ways to extend the observation time. One approach is to follow the droplets of interest.[21] Another technique uses the movement of the microscope stage in the opposite direction to the flow.[17] A further option is to stop the droplets with valves.[22,23]

Here we introduce an image-based FLC algorithm to set ΔP close to zero in the center of ROI (Fig. 1). This allows the droplet to be held in position for a period of time, extending the timeframe for imaging. We chose pressure regulators which have several advantages over syringe-based systems. Firstly, the flow has less fluctuations.[24] Second, the response time to parameter changes is faster.[4,25] Thirdly, sample exchange is straight forward.

We expect that our method will provide a deeper insight into the contents of the microfluidic droplets with high precision. For example, the morphology of cells could be studied or movement patterns analyzed. Furthermore, this basic principle can be extended to complex channel geometries. This provides a new tool for controlling pressure-based droplet microfluidics for lab-on-a-chip systems, where on-demand control and manipulation is paramount.

Experimental

Imaging

Images were captured using a monochrome camera (MQ022MG-CM, XIMEA GmbH, Münster, Germany) with a 10× objective (MPlan, NA 0.25, Olympus, Japan) and a tube lens (AC254-200-A-ML, Thorlabs Inc., Newton, USA). An LED light source (Kern & Sohn GmbH, Balingen-Frommern, Germany) was used for illumination (Fig. 2). The condenser consists of two apertures and two lenses (EO ACH 25 × 30 VIS-NIR, Edmund Optics GmbH, Mainz, Germany). A calibration target (A1L3S3, Thorlabs) was used to determine the spatial resolution by measuring the conversion factor (px μm^{-1}).

Microfluidics

A P2CS pressure controller with pressure and vacuum pump (Biophysical Tools GmbH, Wettin, Germany) was used for microfluidic flow control. The connection to the chip is realized by silicone tubing (inner diameter 1 mm, outer diameter 3 mm, length 30 cm, Carl Roth, Karlsruhe, Germany) and male elbow Luer connectors (10802, ibidi GmbH, Gräfelfing, Germany), which fit onto female Luer to 10–32 UNF threads, which act as sample reservoirs. The interface to the straight channel glass chip (Fluidic design 1072, microfluidic ChipShop GmbH, Jena, Germany), channel dimensions (width: 100 μm, depth: 37 μm, length: 58.5 mm) is realized by a custom 3D printed holder and silicon O-rings for sealing.
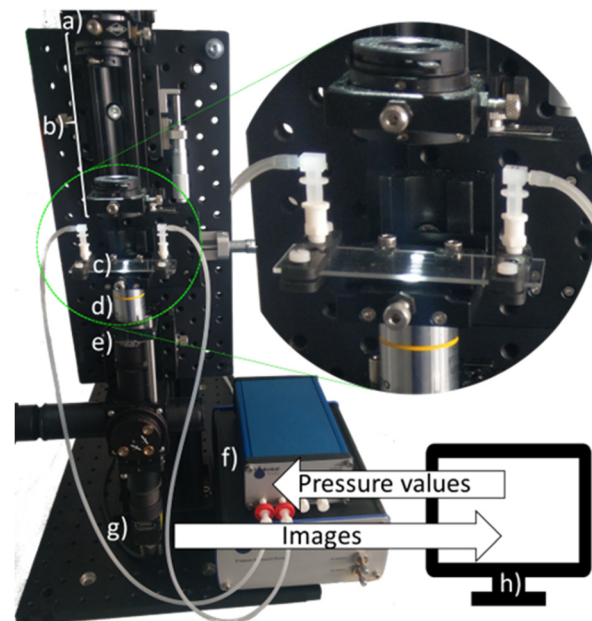

Fig. 2 Experimental setup, a) LED light source, b) condenser, c) microfluidic chip, d) 10× objective, e) tube lens, f) pressure controller with pressure and vacuum pump, g) monochrome camera, h) computer with control software.

Samples

Continuous phase (Pico-Wave 7500 with 0.5% (V/V) Pico-Surf, Sphere Fluidics, Cambridge, UK) was prepared. The disperse phase samples were deionized water (H$_2$O), *Saccharomyces cerevisiae* 250 mg ml^{-1} H$_2$O, diluted 1:1000 and 1:100 in H$_2$O. Droplet generation was performed using a cross-shape channel chip (Fluidic design 82, microfluidic ChipShop GmbH, Jena, Germany) and a 10 ml syringe (B. Braun SE, Melsungen, Germany). During the manual droplet generation, the syringe plunger was randomly pulled with varying speed to produce polydisperse droplets. Respectively 20 μl of these prepared emulsions were pipetted into the inlet sample reservoir of the straight channel chip.

Software

The imaging and pressure control algorithms were developed in the LabVIEW programming environment (LabVIEW 2019, version 19.0.1f5, 64-bit, Vision Development Module, National Instruments Corp., Texas, USA). Fiji[26] was used for image calibration and video editing. OriginPro 2024 (64-bit, version 10.1.0.170, OriginLab Corp., Northampton; USA) was used for graph visualization. Microsoft Office Professional Plus 2019 (Microsoft Corp., Redmond, USA) was used for writing, figure generations and flowcharting.

Microfluidic state machine

The program sequence is implemented by a state machine. The default state is designated as *Manual* which enables the user to modify the values transmitted to the pressure controller. Upon selection of the *Feedback* operation mode,

the state transitions to *Init*. The pressure values p_{inlet} and p_{outlet} are incrementally increased or decreased by *pos_neg_pressure_increment* until *max_pos_neg_pressure* is reached. If both droplet sides, *dLL* and *dRR* are true and $cLx_{inv} + cRx = drop\_length$ is within the range of *min_drop_length* and *max_drop_length* the state switches to *Center*. In the absence of a detection of either *cLx* or *cRx* for a period of one second, the state reverts to its initial state *Init*. The first *Center* loop execution sets p_{inlet} and p_{outlet} to zero. If both *dLL* and *dRR* are true the value of *drop_length/2* will be set as the actual points for the input MSF *contour position*. In turn, the MSF *pressure change* will be modified in accordance with the values of *vL* and *vR*. When either *dLL* or *dRR* is true, the corresponding MISO FLC is executed and the calculated value is added to p_{inlet} and p_{outlet} until *max_pos_neg_pressure* is reached or the *center_stabilizing_timer* is true. This is the case when $cLx_{inv} = x_{leftmax} - drop\_length/2 \pm 5\ px$ or $cRx = drop\_length/2 \pm 5\ px$ are in range for 1 s. The follow-up state is *Hold*, here the pressure values remain constant until the predefined *Hold time* has expired and then the state switches to *For*. Here, similar to *Init* p_{inlet} and p_{outlet} are in-/decreased stepwise until *max_pos_neg_pressure* is reached or droplet side *dRL* becomes true. In this case *n_droplets_done* will be incremented by one and the state changes to *Init*. This cycle continues till *n_droplets_done = Image_n_droplets*, then the sequence lingers into the *Center* state. There is the option to continue the sequence by increasing *Image_n_droplets* or to quit the program.

Droplet contour detection

The readout of the *y*-pixels from the raw camera image is reduced to the width of the microfluidic channel, excluding the channel walls. This equates to 128 pixels. The number of *x*-pixels was set to 512 px and 1024 px. The main ROI camera
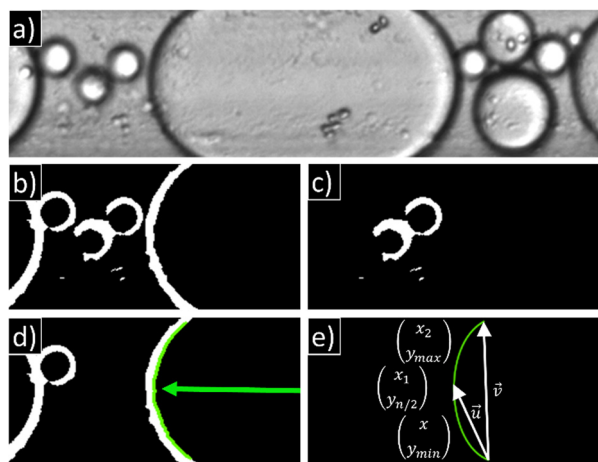

Fig. 3 Image processing steps; a) main ROI camera image; b) cropped, threshold, binary, left ROI; c) rejected border objects; (d) absolute difference between (b) and (c) with first contour detected, search direction right to left; e) b-spline fitting and coordinate pairs for droplet side calculations.

images (Fig. 3a) were divided into two ROI's in *x*-direction, namely the left and right ROI (IMAQ Extract 2.vi). Subsequently, the thresholding of the raw 8-bit greyscale images, which ranged from 0 to 100, was conducted in order to transform them into binary images (IMAQ Threshold.vi, Fig. 3b). Subsequently, the boarder objects are identified (IMAQ RejectBorder.vi) and the resulting image (Fig. 3c) is subtracted from the input image (IMAQ Absolute Difference.vi). The calculated image comprises solely border objects and is employed for the purpose of contour detection. The IMAQ Extract Contour.vi was set to only identify the first contour from search start. The search directions were defined from right to left for the left ROI and from left to right for the right ROI. The contours that have been detected are then overlaid on the images for visualization (Fig. 3d). To achieve a smoother contour data set, a spline curve fitting technique (IMAQ Fit Contour.vi) was employed. In order to exclude false positive results, the pixel array of *xy*-clusters is checked for the criteria $y_{min} \leq 8\ px$ and $y_{max} \geq 120\ px$. In the false case, the position information is set as *Not a Number* (*NaN*) while the droplet sides (*dLL, dLR, dRL, dRR*) are set as *false*. If the aforementioned criteria are met the vector $\vec{u} \times \vec{v}$ is calculated (Fig. 3e). A positive result (>0) indicates that the left side of the droplet has been identified, whereas a negative result (<0) implies that the right side has been detected. Consequently, the droplet side variables were designated as either *true* or *false*. Additionally, the corresponding *x* value to $y_{n/2}$ was utilized as the position (*cLx, cRx*). In order to apply the same fuzzy input membership function (MSF) for both *contour positions*, it is necessary to invert *cLx* whereby $x_{leftmax} - cLx = cLx_{inv}$. The *contour velocity* is calculated only if the same droplet side is detected in two consecutive frames (*vL, vR*).

Fuzzy logic control

Two parallel MISO FLC systems were implemented using the FL Fuzzy Controller (MISO).vi. The input variables are the *contour position* ($c = cLx_{inv}$ or *cRx*) and the *contour velocity* ($v = vL$ or *vR*). In the *Center* state the three triangular-shaped input MSFs *contour position* are programmatically changed to the actual *drop_length/2* (Fig. 4a; *n*: point 3, *z*: point 2, *p*: point 1). The input MSF *contour velocity*, which comprise two trapezoid-shaped *n* and *p* functions and one narrow triangular-shaped *z* function remain unchanged (Fig. 4b). The output MSFs *n* and *p* will be adapted in accordance with the respective speed v = *vL* or *vR* (Fig. 4c). The fuzzy rule base comprises a total of nine rules (Fig. 4d). The defuzzification method employed was the center of maximum. For all rules, the antecedent connective was set to AND (minimum), the degree of support is equal to one and the consequent implication was set to minimum. The output *dp1* and *dp2* are added to p_{inlet} and p_{outlet}.

Results and discussion

A total of 2400 droplets were examined. For each sample (H_2O, *S. cer.* 1 : 1000, *S. cer.* 1 : 100) and main ROI (512 px,
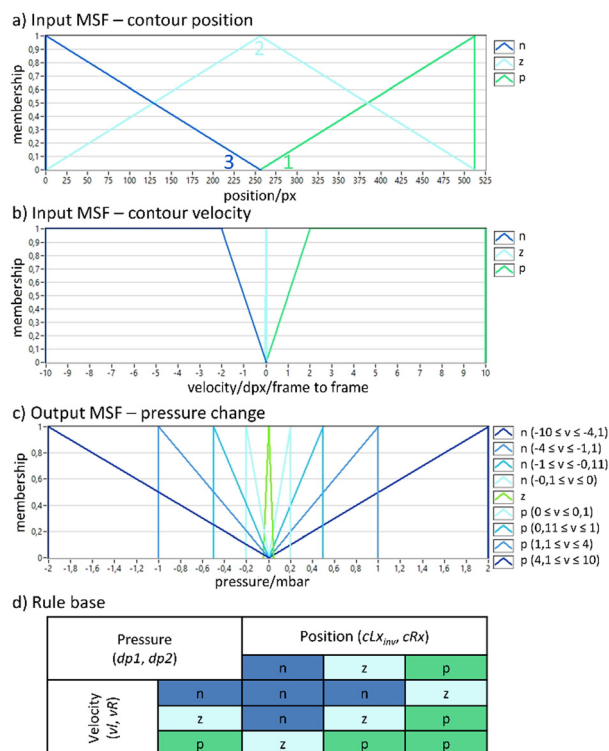
Fig. 4 a) Input MSF – *contour position* for 1024 px main ROI; b) input MSF – *contour velocity*; c) output MSF – pressure change; d) rule base.

1024 px), 400 droplets were processed. The total measurement time was 11 h:29 m:31 s. Subtracting the *hold time* leaves 8 h:19 m:31 s. This yields an average value of 12.5 s for initializing, centering and forwarding a single droplet. Fig. 5a presents the time distribution of the microfluidic states broken down by the sample group.

Init took a total of 3 h:24 m:41 s, the initialization of a droplet takes 5.1 s on average. The initialization time depends on the pressure difference (ΔP) between the inlet and outlet. Alternatively, the maximum ΔP of the pressure regulator could be applied at the beginning instead of gradually increasing it. Then the flow velocity would immediately increase and the droplets would move into the ROI much faster. However, this increases the probability that droplets will pass through the detection area without being positioned. Furthermore, if the distance between the droplets is small, this would facilitate the system to oscillate. Another decisive factor is when a droplet is transported into the channel. If the ratio of continuous to disperse phase is shifted in favor of the disperse phase, the probability that a droplet will flow into the channel increases. As the two phases have different densities, a phase separation occurs in the reservoir and the denser continuous phase (1.61 g cm^{-3}) is therefore transported into the channel first. To test the setup thoroughly, samples with a polydisperse size distribution were prepared for this experiment. This means that an indeterminate number of droplets do not fulfil the differentiation criteria. In case of a sample with a well-defined monodisperse distribution, the limit values can be

set precisely so that every droplet is processed, which reduces the average initialization time.

Center (4 h:15 min:58 s) takes an average of 6.4 s and is therefore the longest process step. A reduction in pressure to zero mbar results in a sudden decrease in the flow rate. The manufacturer of the pressure controller states that both the rise and fall of 100 mbar take 17 ms.[27] In some cases setting p_{inlet} and p_{outlet} to zero is not sufficient to slow down the droplet exactly in the detection area. Ideally, the flow should stop immediately when the pressure difference is set to zero. However, due to the elasticity of the tube connectors, sample reservoir, sealing ring and the microfluidic chip, there is a compliance which causes a delay time before the flow velocity in the microchannel approaches zero.[23] The silicone tubing between the controller and the sample reservoir makes the largest contribution. In order to shorten delay time and thus also response time of the system, the above-mentioned components should have the lowest possible elasticity and the connection distances should be kept as short as possible. If the delay time is too long or the flow velocity is too high, the droplet passes the ROI without being controlled by the FLC. To avoid this case, the rules of the FLC could be further extended, *e.g.* with MSFs for the current pressure and associated rules. However, such an adaptation requires many attempts to optimally adapt the rules to the system. Another potential cause for this phenomenon is that the *center_stablizing_timer* is reset when neither the *cLx* nor *cRx* are detected in a single frame. This issue could be solved by implementing a moving average to suppress false negative detections.

The hold time of 3 h:10 m is specified by the defined hold times of 1 s, 3 s, 5 s and 10 s. However, this hold time can also be specified by the acquisition time defined by the microscope imaging software and synchronized by triggering for the respective imaging modality used. Typical acquisition times for brightfield images are in the range of µs to ms. However, it is planned to combine the application presented here with non-linear imaging modalities such as two-photon excited fluorescence (TPEF) and coherent anti-Stokes Raman scattering (CARS). Depending on pixel dwell time and resolution, acquisition times in the seconds range can be expected for these non-linear modalities.[28,29]

The state *For* (38 m:51 s) lasted on average 1 s. However, the image acquisition process itself can also take several seconds, depending on the resolution and number of images required, for example, in the case of *z*-stacks or time series. In that case the times required for droplet handling and imaging are of comparable order of magnitude. It should be noted that the total acquisition time is not well suited for high throughput approaches with hundred thousand of droplets. Nevertheless, a few hundred droplets can be examined within a reasonable time frame. In the event that a considerable number of samples is present, it is advisable to presort them according to the characteristics of interest.[30,31]

The histogram depicted in Fig. 5b encompasses droplets whose standard deviation (SD) of *droplet_length* between *Center*, *Hold* and *For* was ≤12 px. This comparison of lengths is
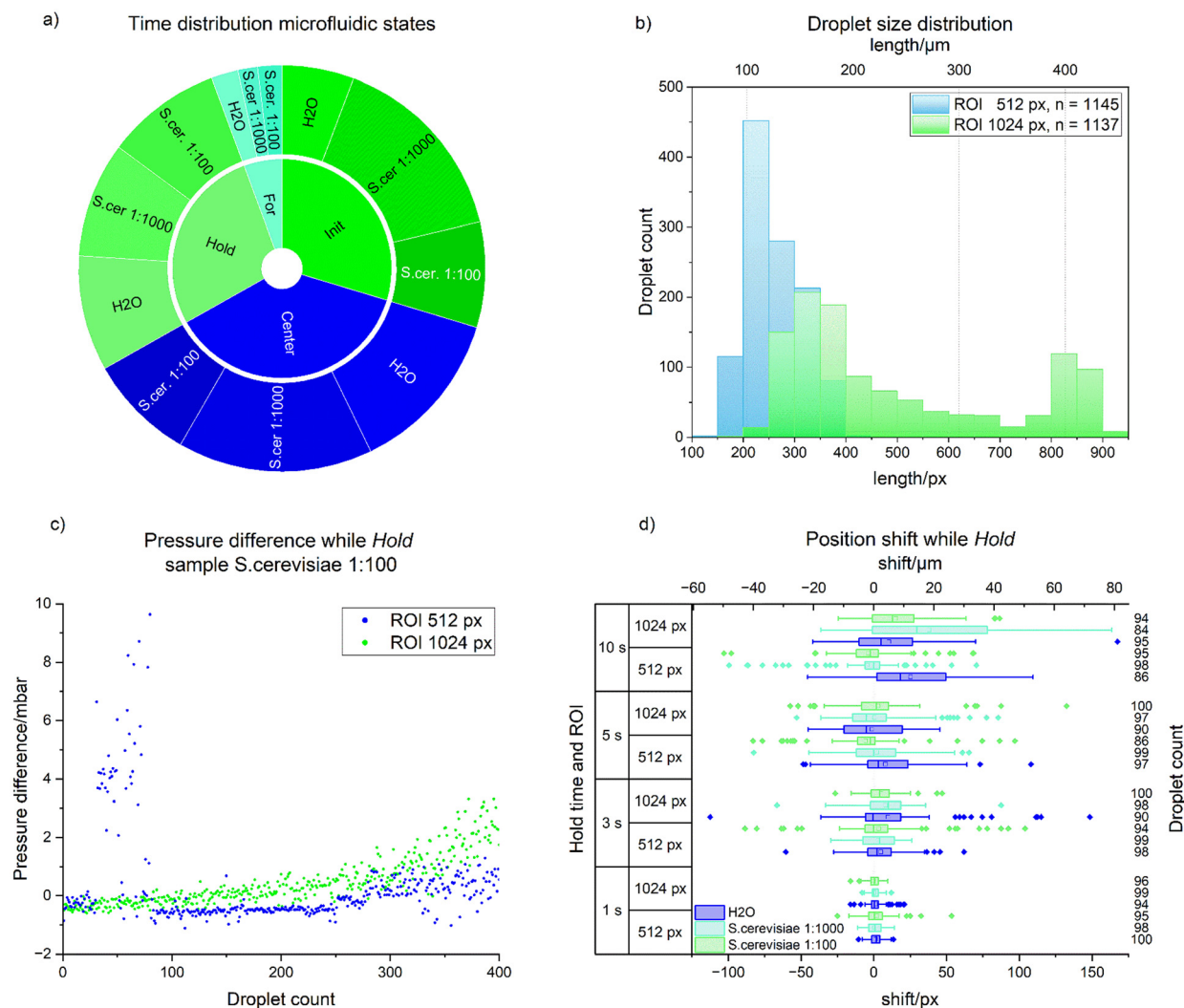
Fig. 5 a) Time distribution microfluidic states; b) droplet size distribution; c) pressure difference while *Hold*; d) position shift while *Hold*.

necessary to eliminate droplets from the evaluation that might have left the detection area during the *Hold* phase or have been caused by false positive contour detection. A total of 55 droplets (ROI 512 px) and 63 droplets (ROI 1024 px) were excluded from the analysis. This means a mean relative error of 4.9% for holding both droplet contours inside the ROI. To reduce this error, the detection could be further improved. Instead of just comparing the droplet contour per frame with the previous, a more robust tracking algorithm could be implemented. A balance should be found between the image processing time and the response time of the microfluidic system. In any case, for the optical system a factor of 2.068 px μm^{-1} was determined with the calibration target. This means that the largest group of 512 px ROI is 109 μm in length. The second largest population with a length of approx. 157 μm belongs to the 1024 px ROI, as does the third largest with 400 μm. The absolute minimum length was 71 μm, and the maximum was 442 μm. This means that *min_droplet_length* and *max_droplet_length* have been undercut and exceeded. The reason for this is that the discriminators decide while *Init*, but the values of the diagram

originate from the *For* state. Another consideration is droplet deformation at high flow velocities, which causes a contour modification between flowing and floating droplets.[20] The length discriminators also serve to achieve a more effective regulation. For this, *min_droplet_length* must be at least 10% greater than the channel width and height. This ensures that it fills the channel cross-section. Similarly, *max_droplet_length* must be at least 10% smaller than the ROI. Otherwise the control distance of the MSF contour position will be insufficient. A simplified approximation is $V_{droplet}$ = droplet_length × width_channel × height_channel for estimating the droplet volume. $V_{droplet}$ extends from 262.7 pl up to 1.6 nl. It is possible to control both smaller and larger volumes, but there are some limitations. These include the channel cross-section, the pressure range of the controller and the ROI defined by the optical system. Furthermore, other pressure controllers can be used with the presented algorithm. If these controllers do not support negative pressures, it is possible to configure the MSFs to an overpressure regime to provide the necessary pressure difference.

The droplets are positioned by the ΔP between the two liquid surfaces in the sample reservoirs (Fig. 5c). This pressure difference results from several factors, including the liquid height in the reservoirs, the channel geometry, the number, size, distribution and composition of the droplets and the continuous phase.[20] A rapid change in ΔP is also an indicator of leaks in the fluidic or pneumatic system. Furthermore, impurities such as dust can lead to an increase. This was almost certainly the case between the 25th and 75th droplet (Fig. 5c, ROI 512 px), where there was a sudden, abrupt increase followed by a drop below the starting level. The system can compensate for impurities of this kind. The controller has a maximum ΔP limitation. If the foreign particle cannot be sufficiently deformed by this differential or exceeds the adhesion force, a blockage will occur in the channel.

The displacement of the droplets during *Hold* (Fig. 5d) is calculated from the averaged difference between cL_{inv} and cR from each first execution of the states *Hold* and *For*. It is clear that the scatter width of the boxplots increases with longer hold time. Furthermore, the data clearly demonstrate that droplet are drifting towards the outlet (Table 1, column: average, minimum, maximum). When grouped by time, it is clear that the SD increases with longer holding times. When the data is grouped according to sample type, it becomes clear that the average shift decreases. The mean and SD increase with increasing ROI size when grouped. This shift has several causes.

Firstly, the values of the pressure controller fluctuate around the set target value. Secondly, the difference in density between the continuous and disperse phases can cause individual droplets to escape from the channel into the reservoirs. This results in a pressure change in the channel. To correct any shifts that occur as a result, the system must be readjusted accordingly. A permanent control can be carried out when imaging in brightfield mode. If the image modality does not allow constant illumination, it can be interrupted for repositioning and continued afterwards. An alternative solution is to implement parallel acquisition of the camera for positioning and other imaging modalities. In conclusion image recognition of the droplet contours is the most important factor for successful positioning. The algorithm is currently designed to recognize the first contour that fulfills the criteria. The response time of the microfluidic controller for the pressure change of ±100 mbar is approx. 17 ms, the communication time between computer and controller is approx. 22 ms. The edge detection and FLC process requires approx. 10 ms. Each pressure value change is based on the analysis of two consecutive images and the edge information obtained from them. Thus, image processing time and response time of the microfluidic controller are on the same time scale. To make the system less error-prone in terms of recognition, all droplet contours in the ROI could be recognized. This would double the FLC MSF *contour position* width, which would also double the control path of the FLC system. This would reduce the probability that a droplet is not detected. However, there is a disadvantage in that it will take longer to process the images. This must be coordinated with the response time of the microfluidic system. The measurements with *S. cerevisiae* have demonstrated that contour recognition is not significantly affected by cellular content and positioning can be carried out successfully. We assume that the functionality remains guaranteed for cell types with the same or smaller diameter and the same or lower cell concentrations. It is clear that higher cell density implies a lower shift during *Hold* (Table 1, group: sample; average). However, further measurements with different cell densities are needed to confirm this assumption.

This system has been designed to analyze in detail pre-sorted droplets from HTS experiments, *e.g.*, in an antibiotic susceptibility assay.[32] In such experiments, millions of droplets are generated and presorting is performed by *e.g.*, fluorescence[33] or elastic light scattering[34] at up to kHz rate, which results in several hundred up to thousand droplets, which need to be automatically analysed in detail.

Another application includes the automated evacuation of pre-sorted droplets from microfluidic chips for transfer to a culture substrate.[35]

Conclusions

The presented system can position a defined number of microfluidic droplets fully automatically in the center of the ROI. The positioning could also be carried out successfully with droplets containing *S. cerevisiae*. In other tests, droplets containing *E. coli* 992 mCherry, *E. coli* 081 GFP, *Microbacteria*, *Bacillus* DSM 1970 were positioned. The selection was programmed to be length-depending, ranging from 150 px to

Table 1 Droplet shift/μm while *hold*

Group	Sample	N	Average	SD	Minimum	Median	Maximum
Time	1 s	582	0.2	3.0	−12.1	0.2	25.9
	3 s	579	1.3	10.8	−54.4	1.7	71.8
	5 s	569	0.3	12.3	−40.1	−0.2	64.1
	10 s	552	3.0	16.9	−49.8	1.9	81.0
Sample	H$_2$O	750	1.7	12.4	−54.4	1.0	81.0
	S. cer. 1 : 1000	772	1.3	12.6	−48.1	0.5	79.1
	S. cer. 1 : 100	760	0.6	10.8	−49.8	0.2	64.1
ROI	512 px	1145	0.7	11.4	−49.8	0.2	52.9
	1024 px	1137	1.7	12.5	−54.4	1.0	81.0

900 px. However, these values are variable and can be adjusted on the software side depending on the expected droplet size. The channel cross-section of the chip allows us to calculate an approximate and calibrated droplet volume of 270 pl to 1.6 nl. However, the system can be easily adjusted to larger and smaller droplet volumes, which are related to the channel sizes of the microfluidic chips. So far, the system has been successfully tested with commercial chips 100 μm wide, 37 μm deep made of glass, 50 μm wide, 50 μm deep made of PMMA (both microfluidic ChipShop GmbH, Jena, Germany), custom glass chips 570 μm wide, 270 μm deep as described previously,[36] and chips made of PDMS of 50 μm channel depth.[37] Thus, the control algorithm is applicable to various droplet volumes, droplet content and chip materials.

Two MISO FLCs are executed in parallel to calculate the pressure values for centering. The average time for initializing, centering and forwarding a single droplet was 12.5 s. This period of time makes it necessary to presort droplets of interest from previous HTS. We successfully held 95.1% of 2400 droplets within the ROI for a *hold time* between 1 s and 10 s. During this time the droplets shifted by an average of 2.5 μm with a standard deviation of 11.9 μm. This is better than recently published stop-flow methods, which result in residual flow velocities of 10–200 μm s^{-1}.[23] In the *hold* span the image modality can be changed and acquisition can be carried out. An advantage of the system is the mobility and access to droplets. This makes it possible to use contained cells for subsequent cultivation after label-free image analysis. We will further develop the system's potential by adapting it to a microfluidic chip capable of generating, merging, storing droplets and observing them at different time points.

Data availability

The data supporting this article have been included as part of the ESI.†

Author contributions

Conceptualization (J. P., T. M.-Z., F. O.), data curation (F. O.), formal analysis (F. O.), funding acquisition (J. P.), investigation (F. O.), methodology (F. O.), project administration (T. M.-Z., M. S., J. P.), resources (J. P.), software (F. O.), supervision (T. M.-Z., M. S., J. P.), validation (F. O.), visualization (F. O.), writing – original draft (F. O.), writing – review & editing (T. M.-Z., M. S., J. P.).

Conflicts of interest

There are no conflicts to declare.

Acknowledgements

References

1 K. Martin, T. Henkel, V. Baier, A. Grodrian, T. Schön, M. Roth, J. M. Köhler and J. Metze, *Lab Chip*, 2003, **3**, 202–207.
2 J. M. Köhler, T. Henkel, A. Grodrian, T. Kirner, M. Roth, K. Martin and J. Metze, *Chem. Eng. J.*, 2004, **101**, 201–216.
3 T. Kawakatsu, Y. Kikuchi and M. Nakajima, *J. Am. Oil Chem. Soc.*, 1997, **74**, 317–321.
4 C. Fütterer, N. Minc, V. Bormuth, J. H. Codarbox, P. Laval, J. Rossier and J. L. Viovy, *Lab Chip*, 2004, **4**, 351–356.
5 M. Joanicot and A. Ajdari, *Science*, 2005, **309**, 887–888.
6 T. Henkel, T. Bermig, M. Kielpinski, A. Grodrian, J. Metze and J. M. Köhler, *Chem. Eng. J.*, 2004, **101**, 439–445.
7 A. Gupta, S. M. S. Murshed and R. Kumar, *Appl. Phys. Lett.*, 2009, **94**, 164107.
8 J. H. Xu, P. F. Dong, H. Zhao, C. P. Tostado and G. S. Luo, *Langmuir*, 2012, **28**, 9250–9258.
9 T. Thorsen, R. W. Roberts, F. H. Arnold and S. R. Quake, *Phys. Rev. Lett.*, 2001, **86**, 4163–4166.
10 X. Wang, Y. Ma, C. Zhang, Y. Pang and Z. Liu, *Exp. Therm. Fluid Sci.*, 2023, **149**, 111019.
11 K. R. Ackermann, T. Henkel and J. Popp, *ChemPhysChem*, 2007, **8**, 2665–2670.
12 A. März, K. R. Ackermann, D. Malsch, T. Bocklitz, T. Henkel and J. Popp, *J. Biophotonics*, 2009, **2**, 232–242.
13 A. Walter, A. März, W. Schumacher, P. Rösch and J. Popp, *Lab Chip*, 2011, **11**, 1013–1021.
14 S. Hengoju, M. Tovar, D. K. W. Man, S. Buchheim and M. A. Rosenbaum, in *Microfluidics in Biotechnology*, ed. J. Bahnemann and A. Grünberger, Springer International Publishing, Cham, 2022, pp. 129–157, DOI: **10.1007/10_2020_140**.
15 J. C. Rolando, E. Jue, N. G. Schoepp and R. F. Ismagilov, *Anal. Chem.*, 2019, **91**, 1034–1042.
16 A. C. Hatch, J. S. Fisher, A. R. Tovar, A. T. Hsieh, R. Lin, S. L. Pentoney, D. L. Yang and A. P. Lee, *Lab Chip*, 2011, **11**, 3838–3845.
17 A. Mehrnezhad, T. J. Kwak, S. Kim, W.-J. Chang and K. Park, *Microsyst. Technol.*, 2019, **25**, 3417–3423.
18 N. R. Beer, K. A. Rose and I. M. Kennedy, *Lab Chip*, 2009, **9**, 838–840.
19 J. D. Tice, H. Song, A. D. Lyon and R. F. Ismagilov, *Langmuir*, 2003, **19**, 9127–9133.
20 C. N. Baroud, F. Gallaire and R. Dangla, *Lab Chip*, 2010, **10**, 2032–2045.
21 M. Kasterke, J. Thien, C. Flake, T. Brands, L. Bahr, A. Bardow and H.-J. Koß, *Fluid Phase Equilib.*, 2023, **567**, 113718.
22 F. Mehmood, Z. Haider, U. Farooq and Y. Baoqun, *Meas. Control*, 2019, **52**, 1517–1531.

23 M. A. Sahin, M. Shehzad and G. Destgeer, *Small*, 2024, **20**, 2307956.

24 Z. Li, S. Y. Mak, A. Sauret and H. C. Shum, *Lab Chip*, 2014, **14**, 744–749.

25 D. F. Crawford, C. A. Smith and G. Whyte, *Sci. Rep.*, 2017, **7**, 10545.

26 J. Schindelin, I. Arganda-Carreras, E. Frise, V. Kaynig, M. Longair, T. Pietzsch, S. Preibisch, C. Rueden, S. Saalfeld, B. Schmid, J.-Y. Tinevez, D. J. White, V. Hartenstein, K. Eliceiri, P. Tomancak and A. Cardona, *Nat. Methods*, 2012, **9**, 676–682.

27 https://biophysical-tools.de/de/microfluidic-flow-control-precision-pressure-control-system/, (accessed 13/05/2024).

28 T. Meyer, N. Bergner, C. Krafft, D. Akimov, B. Dietzek, J. Popp, C. Bielecki, B. Romeike, R. Reichart and R. Kalff, *J. Biomed. Opt.*, 2011, **16**, 021113.

29 D. Akimov, S. Chatzipapadopoulos, T. Meyer, N. Tarcea, B. Dietzek, M. Schmitt and J. Popp, *J. Raman Spectrosc.*, 2009, **40**, 941–947.

30 M. Budden, S. Schneider, G. A. Groß, M. Kielpinski, T. Henkel and J. M. Köhler, *Chem. Eng. J.*, 2013, **227**, 166–173.

31 E. Zang, S. Brandes, M. Tovar, K. Martin, F. Mech, P. Horbert, T. Henkel, M. T. Figge and M. Roth, *Lab Chip*, 2013, **13**, 3707–3713.

32 A. Samimi, S. Hengoju and M. A. Rosenbaum, *Sens. Actuators, B*, 2024, **417**, 136162.

33 S. Hengoju, S. Wohlfeil, A. S. Munser, S. Boehme, E. Beckert, O. Shvydkiv, M. Tovar, M. Roth and M. A. Rosenbaum, *Biomicrofluidics*, 2020, **14**, 024109.

34 A.-S. Munser, M. Trost, S. Schröder, M. Graf, M. A. Rosenbaum and A. Tünnermann, *Appl. Opt.*, 2023, **62**, 411–418.

35 T. Weber, S. Hengoju, A. Samimi, M. Roth, M. Tovar and M. A. Rosenbaum, *Sens. Actuators, B*, 2022, **369**, 132289.

36 K. R. Strehle, D. Cialla, P. Rösch, T. Henkel, M. Köhler and J. Popp, *Anal. Chem.*, 2007, **79**, 1542–1547.

37 M. Tovar, T. Weber, S. Hengoju, A. Lovera, A.-S. Munser, O. Shvydkiv and M. Roth, *Biomicrofluidics*, 2018, **12**, 024115.